Volume 11
Number 28
28 July 2023
Pages 9369–9736

Journal of Materials Chemistry C

Materials for optical, magnetic and electronic devices

rsc.li/materials-c

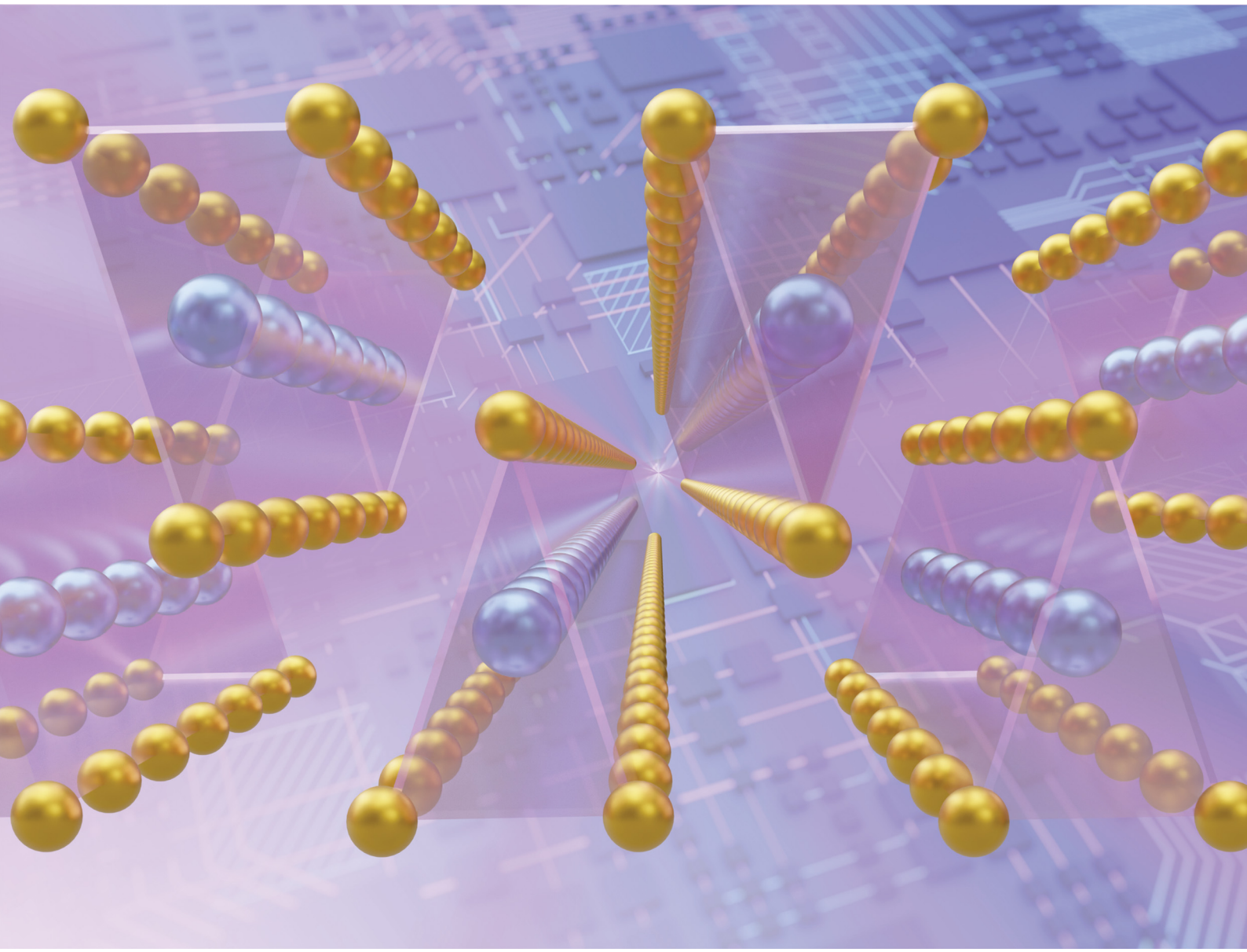

ISSN 2050-7526

ROYAL SOCIETY OF CHEMISTRY

PAPER

Alexey Lipatov, Tula R. Paudel, Alexander Sinitskii *et al.*
Electronic transport and polarization-dependent photoresponse in few-layered hafnium trisulfide (HfS_3) nanoribbons

10 YEARS ANNIVERSARY

Journal of Materials Chemistry C

ROYAL SOCIETY OF CHEMISTRY

PAPER

View Article Online
View Journal | View Issue

Cite this: J. Mater. Chem. C, 2023, 11, 9425

Electronic transport and polarization-dependent photoresponse in few-layered hafnium trisulfide (HfS_3) nanoribbons†

Alexey Lipatov, *[abc] Jehad Abourahma,[a] Gauthami Viswan,[d] Khimananda Acharya,[e] Tula R. Paudel, *[e] Michael J. Loes,[a] Saman Bagheri,[a] Alpha T. N'Diaye,[f] Esha Mishra,[d] Thilini Kumari Ekanayaka,[d] Mohammad Zaz,[d] Jack Rodenburg,[d] Archit Dhingra,[d] Robert Streubel,[dg] Peter A. Dowben[dg] and Alexander Sinitskii *[ag]

We report on the electrical and optoelectronic characterization of field-effect transistor (FET) devices based on few-layered HfS_3 nanoribbons that were mechanically exfoliated from bulk crystals. According to theoretical calculations, bulk HfS_3 crystals require small energies for exfoliation along the (001) planes that are comparable to the cleavage energies of graphene layers from graphite. If measured in air, the devices show a p-type response, which is likely caused by physisorbed and chemisorbed oxygen species. In a vacuum, the devices exhibit n-type conductivity and a large photoresponse to white light and several lasers with wavelengths in the visible range of the spectrum. The device photocurrent exhibited a strong dependence on the direction of polarization, which is related to the highly anisotropic quasi-1D crystal structure of HfS_3. Optical absorption spectroscopy indicates a direct optical band gap of about 2.3 eV and an indirect band gap of about 2 eV. The indirect gap is supported by the band structure that was calculated using density functional theory (DFT). According to the DFT results, direct and indirect band gaps are present in both monolayered and few-layered HfS_3 crystals and decrease with an increase in the number of layers. The absence of strong photovoltaic charging in X-ray photoemission indicates mobile hole carriers. The effect supports the contention that in the presence of light, the photocarriers include both electrons and holes, hence enhancing the photocurrent of the devices. X-ray absorption spectroscopy indicates the S-p–Hf-d hybridization at the conduction band minimum, which is consistent with the calculated band structure.

Received 3rd March 2023,
Accepted 25th May 2023

DOI: 10.1039/d3tc00773a

rsc.li/materials-c

1. Introduction

Group 4 transition-metal trichalcogenides (TMTCs) with a general formula of MX_3, where M is a transition metal, such as Ti, Zr or Hf, and X is a chalcogen, such as S, Se or Te, are receiving increasing attention from the scientific community because of their unique quasi-one-dimensional (quasi-1D) structure, intriguing physical properties, and great potential for emerging optoelectronic applications.[1–3] These TMTC materials are composed of covalently bonded 1D chains of trigonal MX_3 prisms that contain M^{4+} centers surrounded by chalcogenide (X^{2-}) and dichalcogenide (X_2^{2-}) units.[4,5] Bulk TMTC crystals have a highly anisotropic monoclinic structure ($P2_1/m$ space group), as shown in Fig. 1a, with the covalently bonded 1D chains aligned along the crystallographic b direction. Because of the relatively weak interactions between these 1D chains,[6] the Group 4 TMTC materials can be conveniently exfoliated into thin nanoribbon-like flakes with their long axes corresponding to the direction of the chains.

[a] Department of Chemistry, University of Nebraska-Lincoln, Lincoln, NE 68588, USA. E-mail: alexey.lipatov@sdsmt.edu
[b] Department of Chemistry, Biology and Health Sciences, South Dakota School of Mines and Technology, Rapid City, SD 57701, USA
[c] Karen M. Swindler Department of Chemical and Biological Engineering, South Dakota School of Mines and Technology, Rapid City, SD 57701, USA
[d] Department of Physics and Astronomy, University of Nebraska-Lincoln, Lincoln, NE 68588, USA
[e] Department of Physics, South Dakota School of Mines and Technology, Rapid City, SD 57701, USA. E-mail: tula.paudel@sdsmt.edu
[f] Advanced Light Source, Lawrence Berkeley National Laboratory, Berkeley, CA 94720, USA
[g] Nebraska Center for Materials and Nanoscience, University of Nebraska-Lincoln, Lincoln, NE 68588, USA. E-mail: sinitskii@unl.edu

† Electronic supplementary information (ESI) available. See DOI: https://doi.org/10.1039/d3tc00773a

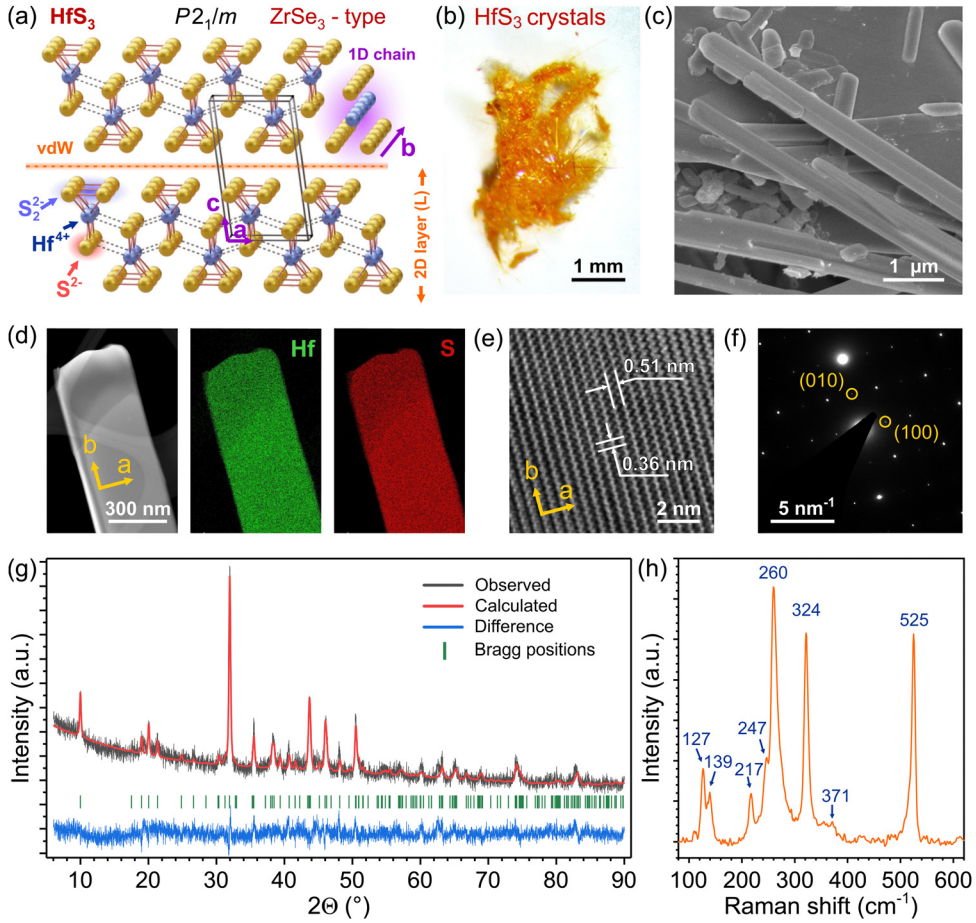

Fig. 1 Characterization of HfS_3 crystals. (a) Scheme of the crystal structure of HfS_3. This monoclinic $ZrSe_3$-type structure with a $P2_1/m$ space group is also typical for other Group 4 TMTC materials. (b) Optical photograph of the as-grown HfS_3 crystals. (c) SEM image of HfS_3 crystals. (d) TEM image of the HfS_3 crystal along with its EDX maps for Hf and S. (e) High-resolution TEM image of the same HfS_3 crystal as in panel (d). (f) SAED image of the same HfS_3 crystal as in panel (d). (g) XRD pattern of the HfS_3 powder accompanied with the results of Rietveld refinement. (h) Raman spectrum of the HfS_3 crystal, measured using a 532 nm laser.

Because of their small thickness, the exfoliated TMTC flakes can be used for the measurements of gate-dependent electrical properties, which in recent years have gained significant interest in the case for TiS_3[7–16] and, to a lesser extent, for ZrS_3.[17–19] In particular, electrical measurements of TiS_3 revealed many interesting characteristics, such as an n-type transport,[7–9] a gate-dependent metal–insulator transition around 220 K,[13] gas sensing properties,[20] and a possible access to charge density wave physics at low temperatures.[2,10,15,21] Compared to TiS_3 and ZrS_3, there were fewer studies on field-effect measurements on exfoliated HfS_3 flakes,[22,23] and some of the basic electronic properties of this material, such as its electrical conductivity and charge carrier mobilities, have not been reported as yet.

The highly anisotropic structure of Group 4 TMTCs also opens interesting opportunities for their optoelectronic applications as charge carriers in these materials can be excited along and across the quasi-1D chains depending on the polarization of the excitation radiation. Polarization-dependent spectroscopic studies of TiS_3, ZrS_3, and HfS_3 revealed strong anisotropy of their Raman signal, optical absorption, and light emission.[18,24–30] From a practical perspective, the anisotropy of the optical properties of TMTCs could be promising for polarization-sensitive photodetectors. All three MS_3 (M = Ti, Zr, and Hf) materials have been tested as potential photodetectors,[7,17,18,22,30–32] but the polarization-dependent photoresponse measurements have only been reported for devices based on TiS_3 and ZrS_3[18,19,25–30] and not for those based on HfS_3.

While much less experimental research has been done on HfS_3 compared to other Group 4 transition-metal trisulfides, it is an interesting material with potential applications in energy storage,[33,34] hydrogen photogeneration,[35] and photodetectors.[22,31,32] There are also intriguing theoretical predictions regarding the tunability of electrical properties of HfS_3 *via* tensile strain[36] and compatibility of HfS_3 with other chalcogenide materials in heterostructures for photovoltaic applications.[37] Further electrical and polarization-dependent photoresponse measurements of HfS_3 are necessary to provide more insights into the electronic and optoelectronic properties of this material as well as to enable exploration of its device applications. In this study, we

report on the electrical characterization of field-effect transistors (FETs) based on exfoliated few-layered HfS_3 nanoribbons and show that they exhibit a highly polarization-dependent photoresponse, similar to devices based on other anisotropic quasi-1D chalcogenide materials.[18,19,25,30,38]

We also provide computational insights into the properties of HfS_3 that are relevant to device fabrication and electrical measurements. We employed density functional theory (DFT) to calculate the cleavage energies for HfS_3 and theoretically confirm that the exfoliation of HfS_3 flakes from bulk crystals should be a facile process. We also used DFT to demonstrate that direct and indirect band gaps are present in both monolayered and few-layered HfS_3 crystals and decrease with an increase in the number of layers.

In addition to the experimental polarization-dependent photoresponse measurements of HfS_3 devices, we also attempted to gain insights into the photoexcitation process by a spectroscopic study of the unoccupied states of HfS_3. The band structures of TMTCs, which are necessary for the understanding of electrical and optical properties, have been discussed in several studies. Theoretical calculation of band alignment using DFT carried out for monolayers of ZrS_3, HfS_3, and their heterostructures indicated that their valence band maximum is dominated by the p state of the chalcogen, whereas the conduction band minimum is dominated by the d state of the transition metal.[37] An in-depth study of TiS_3 and ZrS_3 by observing the unoccupied and occupied states above and below the Fermi level found through experiments and theory indicated that the unoccupied states of the conduction band are dominated by s–d or p–d hybridization,[39] consistent with previous predictions.[40] While there are photoemission studies of HfS_3,[23] a systematic study of the unoccupied states of HfS_3 is absent and would be valuable for a better understanding of the optical excitation process.[39]

2. Results and discussion

HfS_3 crystals were prepared *via* a direct reaction between elemental hafnium and sulfur at 650 °C in a vacuum-sealed ampoule, as described in the Experimental section. The as-grown crystals were up to about 1 mm long and had a bright-orange color, as shown in the optical photograph in Fig. 1b. In addition to the large mm-scale HfS_3 crystals visible in Fig. 1b, there were also multiple smaller whiskers that are shown in the scanning electron microscopy (SEM) image in Fig. 1c. A typical transmission electron microscopy (TEM) image of a HfS_3 crystal is shown in Fig. 1d. Energy-dispersive X-ray (EDX) spectroscopy performed on this crystal shows a uniform distribution of Hf and S, as seen in Fig. 1d, further confirming the composition and purity of the HfS_3 sample. A high-resolution TEM (HRTEM) image of the crystal is shown in Fig. 1e. It reveals high crystallinity of the material and shows the interplane distances of about 0.51 nm and 0.36 nm, which correlate well with a and b lattice parameters of the HfS_3 crystal structure, respectively.[4,5] Based on these measurements, the long axis of this crystal corresponds to the crystallographic b direction of quasi-1D chains, while the lattice parameter a is perpendicular to it, as shown by the orange arrows in Fig. 1e. The crystallographic orientation of this crystal can also be determined from a selected area electron diffraction (SAED) pattern, as seen in Fig. 1f. Both (100) and (010) diffraction spots can be seen in the SAED pattern in Fig. 1f, and their positions match the a and b unit cell parameters, respectively, confirming the orientation of the crystal shown by the reference frame in Fig. 1e. Based on the HRTEM and SAED results, the same crystallographic observations were made for several other HfS_3 crystals, such that their long axes corresponded to the crystallographic b direction of quasi-1D chains, while their thinnest dimensions corresponded to the c direction.

Some of the HfS_3 crystals were ground using an agate mortar and pestle, and the resulting powder was characterized by X-ray diffraction (XRD). The powder XRD pattern in Fig. 1g shows that HfS_3 is highly crystalline and no additional peaks representing any other phases were detected. The lattice constants extracted by the Rietveld analysis are a = 0.5114(1) nm, b = 0.3608(1) nm, c = 0.8974(2) nm, and cant angle β = 97.71(1)°; these values are in good agreement with the previously reported data.[4,5] A representative Raman spectrum of a HfS_3 crystal (Fig. 1h), which was measured using a 532 nm laser, is also consistent with the previously reported results.[24,41,42] While we did not investigate the effect of anisotropy of HfS_3 crystals on their Raman response, it was previously established to depend on the direction of polarization of the excitation laser relative to the crystallographic b direction of quasi-1D chains.[24,41]

Because of the large Z of Hf, we included the effect of spin–orbit coupling (SOC) in the DFT calculations of the band structures of monolayered and bulk HfS_3. The results are presented in Fig. 2a and b for calculations without and with SOC, respectively. In bulk crystals and with SOC, the main feature of the band structure includes an indirect fundamental band gap of 1.40 eV with the valence band at $k = \pm 0.06$ Å^{-1} and the conduction band at the X-point of the Brillouin zone, that is, along the chain direction. The direct band gaps at Γ- and X-points are larger than the indirect fundamental band gap by 0.19 eV and 0.04 eV and have values of 1.59 eV and 1.44 eV, respectively. The indirect nature of the band gap is consistent with a significant tail in optical absorption, as discussed below. Fig. S1 (ESI†) shows the evolution of band structures when the thickness of HfS_3 increases from one to six monolayers. Fig. 2c summarizes these results and shows the evolution of the fundamental band gap and the direct band gaps at Γ- and X-points of the Brillouin zone. The nature of the band structure remains the same upon changing the thickness of a HfS_3 crystal, even though the band gap slightly increases upon decreasing thickness from 1.40 eV in the bulk to 1.62 eV in a monolayer, which indicates relatively weak quantum confinement effects.[43] The calculated effect of SOC results in the overall band gap reduction by 14 meV in the bulk and 6 meV in a monolayer. The direct band gap at the Γ-point also shows a weak confinement effect, whereas the band gap at the X-point shows stronger confinement effects. The observed effect is

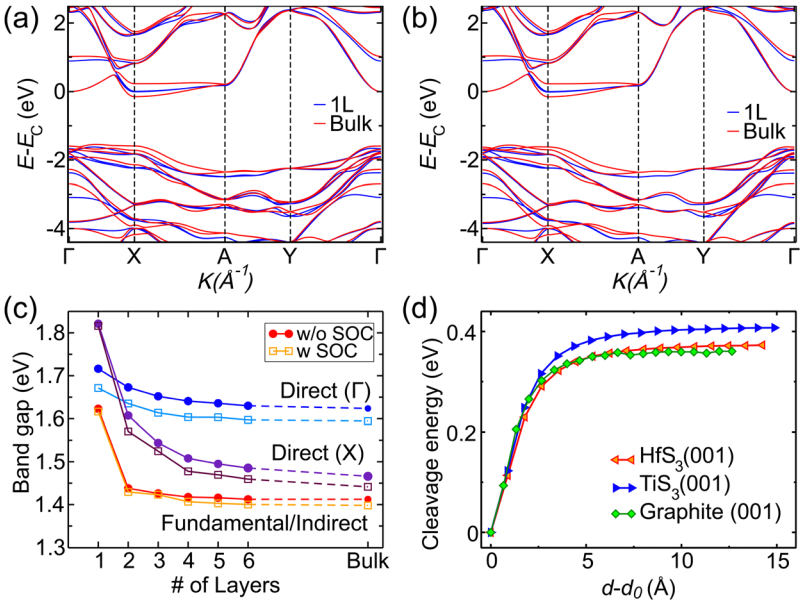

Fig. 2 Cleavage energy and band structure of HfS_3. (a and b) Comparison of band structures for monolayered and bulk HfS_3 crystals (a) without and (b) with spin–orbit coupling. In each band structure, the conduction band minimum at the center of the Brillouin zone was used as the zero-energy level. (c) Evolution of the HfS_3 band gap as a function of the number of layers. The results are shown for direct and indirect band gaps calculated with and without spin–orbit coupling. (d) Cleavage energy calculations for the HfS_3 crystal along the (001) plane plotted as a function of plane separation. Similar cleavage energies for graphite and TiS_3 calculated using the same computational approach are shown for comparison.

related to the stronger weight of the orbitals like d_{z^2} and p_z with the lobes pointing to the confinement direction at the *X*-point.

Few-layered HfS_3 flakes for the device fabrication were prepared *via* mechanical exfoliation of bulk crystals using adhesive tape.[44] We previously applied the same exfoliation procedure to TiS_3 crystals to produce thin flakes and study their properties.[6,8,45] When layers of HfS_3 or TiS_3 were peeled from bulk crystals using adhesive tape and then transferred onto Si/SiO_2 substrates, it was noticeable that the exfoliated HfS_3 flakes were more commonly found compared to similarly prepared TiS_3 flakes. In order to support this experimental observation, we employed DFT to calculate the energies required for the separation of a single layer from a bulk crystal of HfS_3 or TiS_3. Similar calculations were also performed for the exfoliation of a single graphene layer from a graphite crystal, which was used as a reference representing a prototypical two-dimensional (2D) material. Fig. 2d shows the calculated cleavage energies for the (001) planes of HfS_3, TiS_3 and graphite crystals as a function of the layer separation. The energies required for the complete cleavage of 2D layers from crystals of HfS_3 (0.36 J m^{-2}) and TiS_3 (0.39 J m^{-2}) were found to be comparable to the cleavage energy of graphene (0.35 J m^{-2}), suggesting that both TMTC materials should be relatively easy to exfoliate. The slightly smaller calculated cleavage energy of HfS_3 compared to TiS_3 also agrees with the experimental observations. The calculated energy for the cleavage perpendicular to the *b* direction of the quasi-1D chains (Fig. 1a), that is, for the (010) planes of HfS_3 crystal, is 2.50 J m^{-2}, which is much larger than that for the (001) planes. This result agrees with the previous study of the exfoliation of TiS_3,[6] which demonstrated that the cleavage proceeds along the planes that split a crystal between the weakly interacting quasi-1D chains, such as the (001) plane, while the cleavage across these chains that breaks their covalent bonds (*e.g.*, the (010) plane) would be much more energetically expensive. Because the cleavage across the quasi-1D chains is unlikely, the TMTC crystals typically exfoliate into thin nanoribbon-like flakes with their long axes corresponding to the *b* direction of the chains. It should be noted that the cleavage energy results for TiS_3 and graphite slightly deviate from those reported previously in ref. 6, 46 due to the use of DFT-D3 dispersion corrections, which provide more accurate results for interlayer separation.[47] However, all qualitative conclusions regarding the general ease of exfoliation of TMTC materials or the relative differences between different cleavage planes appear to be the same for both computational approaches.

Several field-effect transistor devices based on HfS_3 were fabricated to study its optoelectronic properties. A device scheme is shown in Fig. 3a, and it depicts an exfoliated HfS_3 flake bridging source (S) and drain (D) 60 nm-thick gold electrodes. The devices were fabricated on a heavily p-doped Si substrate covered with a 300 nm-thick layer of dielectric SiO_2. The conductive Si layer served as a global gate (G) electrode in electrical measurements. The microscopic optical image of one of the devices is shown in Fig. 3b and demonstrates that thin exfoliated HfS_3 flakes that were used for device fabrication appeared blue on a Si/SiO_2 substrate rather than orange as in bulk crystals. To measure the flake thickness, we employed atomic force microscopy (AFM) in the tapping mode. The resulting image is demonstrated in Fig. 3c with the corresponding height profile of the flake shown

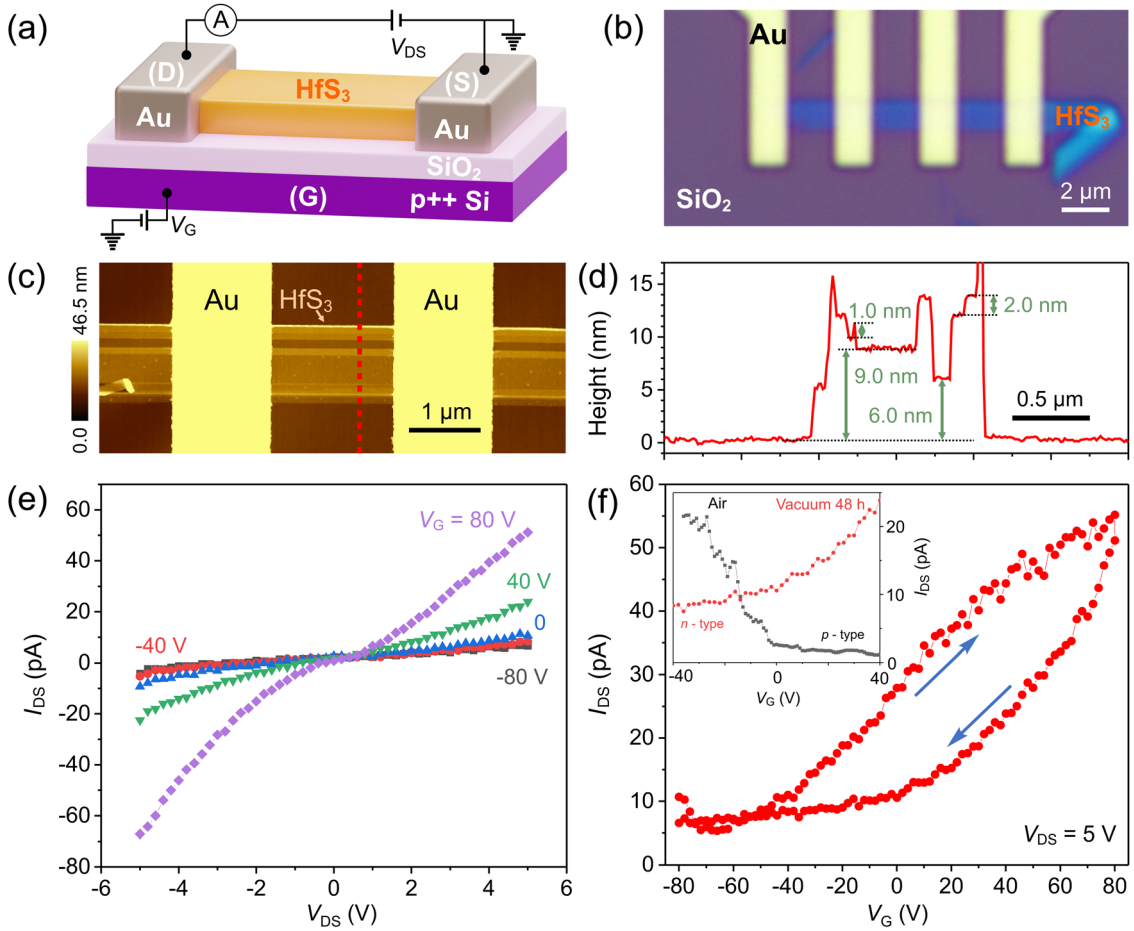

Fig. 3 Electronic properties of HfS_3 single crystals. (a) Scheme of the HfS_3 FET device. (b) Optical image of the HfS_3 device with four gold electrodes. (c) AFM image of the central segment of the device shown in panel (b). The Au electrodes are colored in yellow because their thickness (60 nm) exceeds the height range. (d) Height profile measured across the HfS_3 device channel along the red dashed line in panel (c). (e) I_{DS}–V_{DS} curves measured in a vacuum at different gate voltages for the HfS_3 device shown in panel (c). The measurements were performed under white light illumination. (f) Transfer characteristics for the same HfS_3 device recorded in a vacuum at V_{DS} = 5 V. The inset shows that the transfer characteristics of HfS_3 devices change depending on whether the measurements are performed in air or in a vacuum, revealing either p- or n-type behavior, respectively.

in Fig. 3d. The profile reveals an uneven thickness of the HfS_3 flake with heights ranging from 5 to 16 nm. It is notable that the flake has several parallel terraces with a minimal step height of about 1 nm, which is in good agreement with the *c* lattice parameter of the HfS_3 structure. Similar features were observed in the AFM images of other anisotropic quasi-1D trichalcogenide materials, such as TiS_3[6] and In_4Se_3.[38] We estimate the average thickness of this flake to be about 10.5 nm, while the length and the width of the HfS_3 channel in this device segment are 1.7 μm and 1.1 μm, respectively.

Prior to electronic transport measurements, the device was kept in a vacuum chamber of a probe station at a base pressure of about 2×10^{-6} Torr for at least 48 h. The long evacuation was important to desorb molecular adsorbates, such as water molecules, that deposit on devices when they are exposed to air.[48] We have previously shown that the removal of these surface adsorbates is important to reveal the intrinsic n-type character of the transport in HfS_3, which appears to be p-type if measured in air.[23] The electronic transport was assessed under white light illumination using a two-terminal device configuration, and the drain–source current (I_{DS}) was measured with varying drain–source voltage (V_{DS}) and gate voltage (V_G). Fig. 3e shows I_{DS}–V_{DS} curves measured at different V_G values ranging from −80 V to +80 V. The I_{DS}–V_{DS} curves show nonlinear behavior originating from non-Ohmic contacts between the metal of electrodes and semiconductor HfS_3.[23] Under white light illumination, the resistivity of the device shown in Fig. 3b was 6.3×10^{10} Ω sq^{-1} at V_G = 80 V and 3.0×10^{11} Ω sq^{-1} at V_G = 0. When the electrical conductivity was assessed in darkness, the device did not show a measurable current.

The transfer characteristics, or the I_{DS}–V_G dependences of the HfS_3 device, were recorded at V_{DS} = 5 V, as seen in Fig. 3f. The I_{DS} of the device is about 5 pA at V_G = −80 V, but it increases to about 55 pA at V_G = 80 V, resulting in an ON/OFF ratio of 11. The increase of the device current with the gate voltage is consistent with the n-type conductivity of HfS_3.[23] The HfS_3 devices also exhibit a significant hysteresis in the transfer characteristics (Fig. 3f), which is a common feature of FET

devices based on trichalcogenides and is caused by charge trapping of electrons, primarily at the SiO_2 interface. The field-effect mobility (μ_{FE}) was calculated using the formula $\mu_{FE} = C_d^{-1} \times \partial\rho^{-1}/\partial V_G$, where C_d is the capacitance of a 300 nm-thick SiO_2 dielectric layer and ρ is the resistivity of the HfS_3 device channel. The mobility extracted from the slope of the room-temperature I_{DS}–V_G dependence is 1.2×10^{-5} cm^2 V^{-1} s^{-1}, which is on the same order of magnitude as the reported mobilities for ZrS_3.[49] We made an attempt to perform four-terminal measurements to eliminate the effect of contact resistance, as shown in Fig. 3b. However, due to the overall low conductivity, these measurements were not successful. The low ON/OFF ratios and field-effect mobilities in the tested devices could be related to the non-Ohmic contact between HfS_3 and Au contacts,[23] and further research on contact materials for HfS_3 could lead to improved transport properties.

The inset in Fig. 3f demonstrates the effect of the environment on the transfer characteristics of HfS_3 devices. The red curve in the inset in Fig. 3f shows an I_{DS}–V_G dependence for the HfS_3 device, which was measured in a vacuum and demonstrated the n-type transport. However, when a HfS_3 device is measured in air, it shows a p-type behavior, as demonstrated by the black curve in the inset in Fig. 3f. This has been explained by the physisorption of molecular species, such as H_2O and O_2, on the surface of HfS_3.[23] These adsorbates are known for their p-doping effect on other 2D materials, such as reduced graphene oxide, which also exhibits p-type transfer characteristics when measured in air[50–52] but shows an ambipolar behavior when measured in a vacuum.[48,51–53] Similarly, evacuation of a HfS_3 device at about 2×10^{-6} Torr for 48 h results in the removal of the majority of physisorbed oxygen species from the surface of HfS_3, restoring the n-type behavior (Fig. 3f). It is important to note that while the volatile oxygen species could reversibly adsorb and desorb, there is also chemisorbed oxygen on the surface of HfS_3 device channels with a similar p-type doping effect.[23] Therefore, while the measurements performed in a vacuum demonstrate the overall n-type behavior, the hole contribution to the transport properties of HfS_3 cannot be disregarded, especially for device channels based on few-nm-thick nanoribbon-like crystals with a high volume fraction of a partially oxidized surface layer.

For an investigation of the optical properties of HfS_3, we prepared its suspension in ethyl acetate. The as-prepared HfS_3 crystals were sonicated in ethyl acetate, which was preliminarily dried using a 3 Å molecular sieve to prevent oxidation of the material. Likewise, during the sonication, the solvent with the HfS_3 crystals was kept in a tightly sealed round-bottom flask under continuous bubbling of inert Ar gas. After sonicating for 24 h, the suspension was transferred to a separate vial. The resulting suspension of HfS_3 exhibited an orange color, as shown in the inset of Fig. 4a. The concentration of the HfS_3 suspension was determined to be 4 mg mL^{-1}. The UV-vis-NIR absorption spectrum of a freshly prepared HfS_3 suspension is shown in Fig. 4a. The optical absorption significantly decreases when the wavelength of visible light increases (*i.e.*, energy decreases), and the blue and green lights absorb better than the red light; hence, the bright-orange color of the HfS_3 crystals is observed. The Tauc plot drawn in $h\nu - (\alpha h\nu)^2$ coordinates (Fig. 4b) reveals the optical direct band gap of HfS_3 of about 2.3 eV. Similarly, from the plot in $h\nu - (\alpha h\nu)^{1/2}$ coordinates, we conclude that HfS_3 has an indirect band gap of about 2.0 eV (Fig. 4c). The results are in line with the previously reported values, which for the optically measured direct band gap are in the range from 2.2 eV[31,35] up to 3.0 eV[54] and for the indirect band gap are in the range from 1.73 eV[31] to 2.1 eV.[54] Furthermore, the DFT calculations (Fig. 2a–c) also predicted the existence of direct and indirect band gaps in HfS_3, which is consistent with the spectroscopic observations.

The optical band gap of HfS_3 at modest photon energies in the visible region offers an opportunity to study the modulation of electrical conductivity of HfS_3 FETs, that is, photoconductivity, as a function of various photon energies. The photocurrent measurements obtained on the HfS_3 device shown in Fig. 3c are presented in Fig. 5. Fig. 5a shows the photocurrents induced in this device by three different visible lasers, red (685 nm), green (520 nm), and blue (406 nm), which were set at the same power of 0.5 mW. All three lasers induced photocurrent in the device. However, while the use of the blue and green lasers resulted in very reproducible cycles with I_{DS} ON/OFF ratios of 1000 and 500, respectively, the photocurrent in the presence of 0.5 mW red laser is barely noticeable (the ON/OFF ratio is 2). This observation

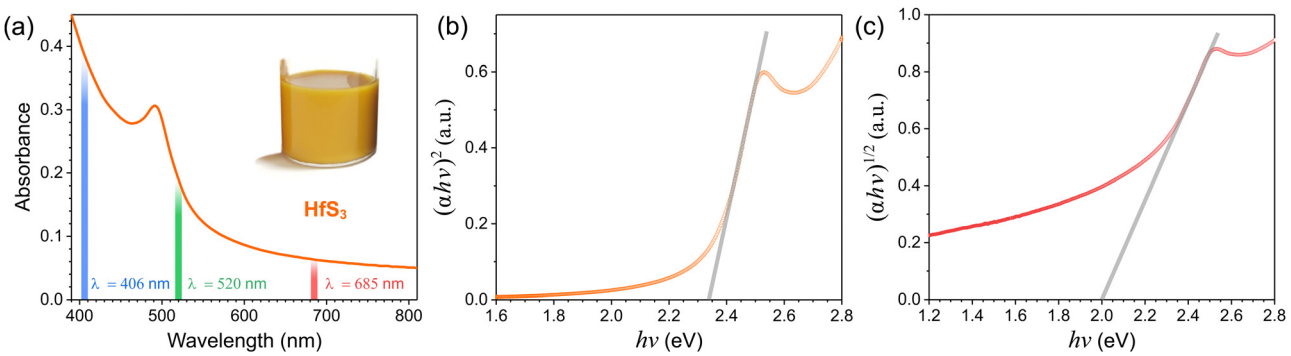

Fig. 4 Optical properties of HfS_3. (a) Optical absorbance spectrum of the HfS_3 suspension in ethyl acetate. Inset: A photograph of a vial with the HfS_3 suspension in ethyl acetate. (b and c) Tauc plots of the spectrum shown in panel a (b) in $h\nu - (\alpha h\nu)^2$ coordinates and (c) in $h\nu - (\alpha h\nu)^{1/2}$ coordinates, where α is the absorption coefficient. The gray lines are linear fits that were used for the band gap assessment.

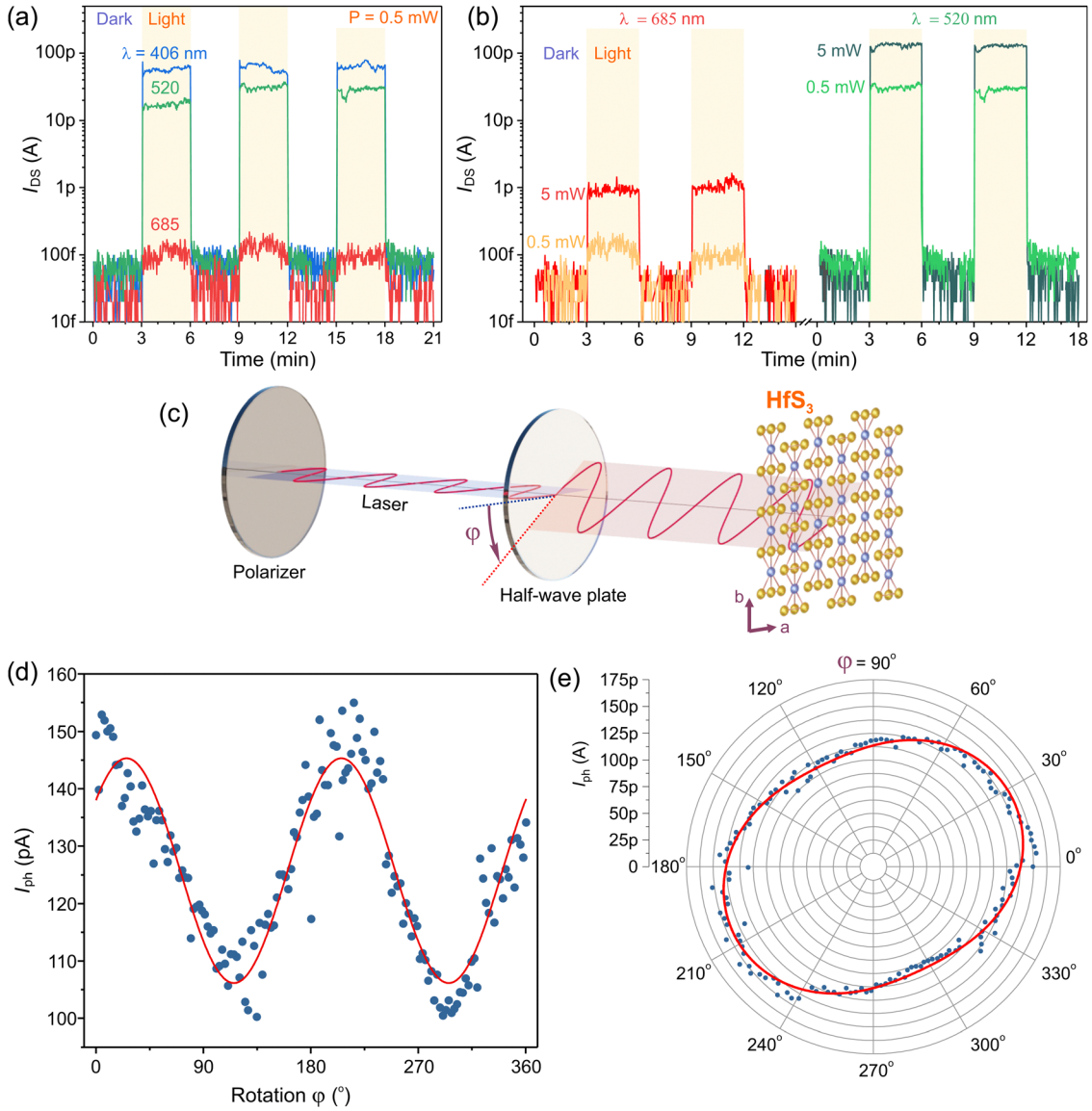

Fig. 5 Optoelectronic properties of HfS_3 devices. (a) The modulation of photocurrent in the HfS_3 device with three different lasers, red (685 nm), green (520 nm), and blue (406 nm). All lasers were set at the same power of 0.5 mW. The measurements were performed at V_{DS} = 5 V and V_G = 0. (b) The modulation of photocurrent in the HfS_3 device with red (685 nm) and green (520 nm) lasers at the power set at 0.5 mW and 5 mW. The measurements were performed at V_{DS} = 5 V and V_G = 0. (c) Scheme of the optical excitation of HfS_3 devices in the polarization-dependent photocurrent measurements. (d) Dependence of photocurrent in the HfS_3 device on the polarization angle of the green laser, set at the power of 5 mW. (e) The 2D contour plot of the photocurrent dependence of HfS_3 on the polarization angle of the green laser, set at the power of 5 mW.

correlates well with the UV-vis-NIR spectrum of HfS_3 solution (Fig. 4a), which shows that the blue and green parts of the visible spectrum have significant light absorption, while the red (685 nm) laser has a lower energy than the direct optical band gap (2.35 eV or 528 nm) of HfS_3. However, the energy of the red laser is close to the measured indirect gap, suggesting the possibility of some optical excitations at 685 nm. In addition, defects and the p-type layer at the surface of HfS_3 caused by the surface oxidation[23,55] could add states at the band edge, making the HfS_3 optically active at energies lower than the band gap. Thus, the generation of photocarriers using the red light source is plausible and consistent with the laser energy-dependent phototransistor measurements, which show very small photoresponse at 685 nm compared to the green and blue lasers with energies larger than the direct optical band gap of HfS_3.

There is also a noticeable dependence of photocurrent on laser power. Fig. 5b shows the photoresponse of the HfS_3 device to red and green lasers at 0.5 mW and 5 mW. The I_{DS} currents for both lasers benefit from increased power, which enhances the photocurrent by orders of magnitude.

The experimental setup for the optical photoconductance anisotropy measurements is shown in Fig. 5c. In brief, a polarized laser beam was focused on the HfS_3 device channel, and the polarization angle (φ) was controlled by rotation of a

half-wave plate. The angle-resolved photogenerated current ($I_{ph} = I_{DS}^{Light} - I_{DS}^{Dark}$) at V_{DS} = 5 V as a function of φ is shown in Fig. 5d for the green laser at a power of 5 mW. The photocurrent exhibits sinusoidal dependence on the incident polarization angle and can be fitted by the following equation:

$$I_{ph}(\varphi) = I_{max}\cos^2(\varphi - \theta) + I_{min}\sin^2(\varphi - \theta) \quad (1)$$

Here, I_{max} and I_{min} represent the maximum and minimum photocurrents, respectively, φ (°) is the angle of rotation of the linearly polarized incident light as shown in Fig. 5c, and θ (°) is the rotation angle at which the *E*-field is parallel to the crystallographic *b* axis of the HfS_3 channel. For the excitation source of 520 nm, I_{max} = 148.0 pA and I_{min} = 104.2 pA, which result in the dichroic ratio I_{max}/I_{min} = 1.42 for the green laser. The dependence of the photocurrent on the polarization angle is also presented as a 2D contour plot (Fig. 5e, scattered data points) along with its fit (red curve) using eqn (1).

The temperature-dependent X-ray photoelectron spectroscopy (XPS) measurements of HfS_3 crystals provide some insight into the type of charge carriers that contribute to the photocurrent. Fig. 6a and b show XPS spectra of S 2p and Hf 4f core levels, respectively, measured at temperatures varying from 180 to 300 K. The S 2p spectrum at 180 K was fitted with four peaks which correspond to S^{2-} $2p_{3/2}$, S^{2-} $2p_{1/2}$, S_2^{2-} $2p_{3/2}$, and S_2^{2-} $2p_{1/2}$ at 161 ± 0.1 eV, 162.2 ± 0.1 eV, 162.2 ± 0.1 eV, and 163.4 ± 0.1 eV, respectively.[23] Of key significance is that X-ray photoemission core level peaks exhibit very little shift in binding energy with decreasing temperature. The emission of electrons during the data acquisition in the photoemission process leads to a positive charge build-up on or near the sample surface, that is, photovoltaic charging, in both insulators and semiconductors.[56,57] The charging, in turn, is known to shift the measured spectral positions of XPS peaks. This effect should be especially pronounced at low temperatures, where the mobility of the surface charge carriers is expected to decrease, hence shifting and distorting the XPS peaks.[56,57] The normal incidence XPS spectra of S 2p and Hf 4f core levels exhibit a negligibly small shift in the peaks at different temperatures. This negligible photovoltaic charging in XPS indicates that recombination is suppressed at the HfS_3 sample surface, and the hole mobility is significant, consistent with the light hole masses.[37,58] The inference is that conventional photoexcitation creates both electrons and holes, with significant conductance contribution due to the hole carriers. Significant hole mobility suppresses surface charging effects caused by the trapped charges on the surface of the HfS_3 sample.

Understanding the electronic structure of the conduction band assists in the understanding of the optical excitations.[38] X-ray absorption spectroscopy (XAS) provides a tool to probe the electronic bands contributing to the unoccupied density of states in trichalcogenides.[39] Fig. 7 shows the XAS spectra taken for the 2p core level edge of S and the $4d_{5/2}$ edge of Hf. The Fermi level (E_F) has been placed at the base point of the absorption peak in a similar way as in the analysis of absorption edge spectra of TiS_3 and ZrS_3.[39] The XAS S 2p core level spectrum (Fig. 7a) has been fit with four peaks, which we attribute to the Hf 5d contributions to the bottom of the conduction band. The p → p optical transitions are not allowed, which means that within 1 eV of the conduction band bottom, the sulfur-weighted 3p states are strongly hybridized with the Hf 5d, as indicated in the calculated HfS_3 band structure in Fig. 8. The effect is similar to the metal d to chalcogenide p hybridization in TiS_3 and ZrS_3.[39] Extra atomic excitations can circumvent optical selection rules so long as the angular momentum of the hybrid band allows for Δl = +1.[59] As seen in the Hf $4d_{5/2}$ edge spectrum in Fig. 7b, there are

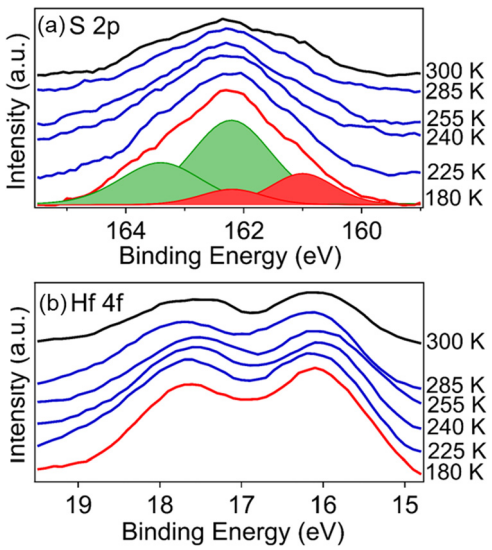

Fig. 6 The temperature-dependent XPS spectra of HfS_3. (a and b) XPS spectra of (a) S 2p and (b) Hf 4f taken at different temperatures as indicated. The core-level components of the S 2p core level shown in the shaded region correspond to S^{2-} $2p_{3/2}$ and S^{2-} $2p_{1/2}$ (both in dark red shade) and S_2^{2-} $2p_{3/2}$ and S_2^{2-} $2p_{1/2}$ (both in green shade).

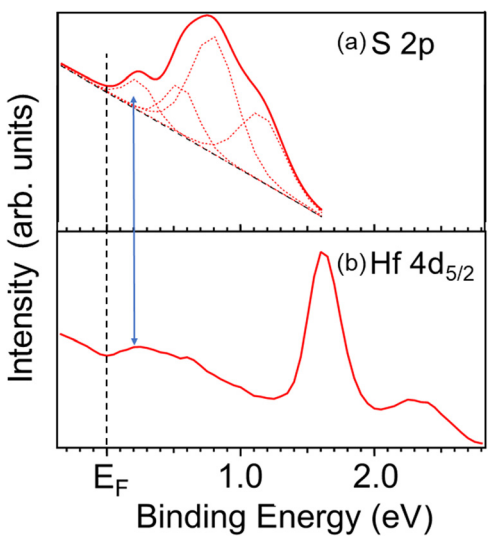

Fig. 7 X-ray absorption spectra of HfS_3. Absorption edge spectra for (a) S 2p and (b) Hf $4d_{5/2}$ placed relative to the Fermi level, which is marked using a vertical black dashed line.

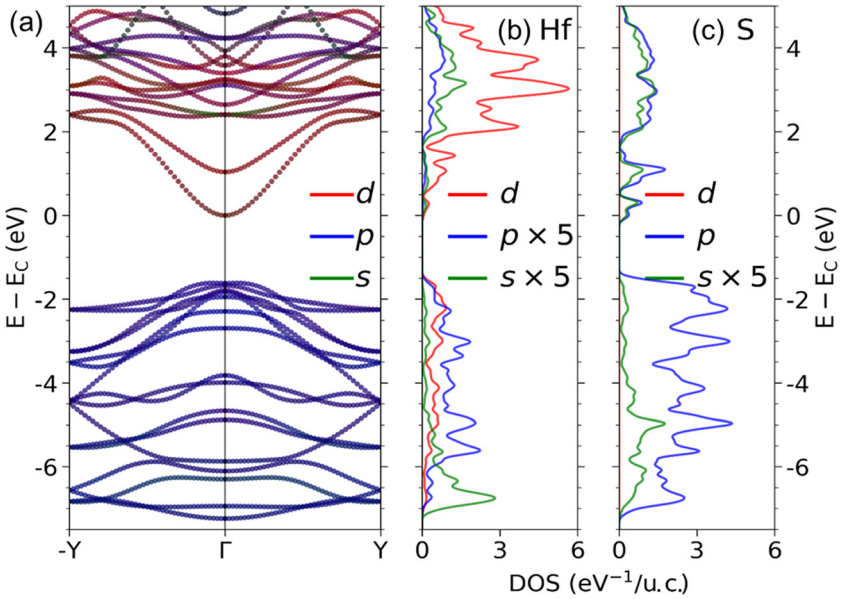

Fig. 8 Electronic structure of HfS_3. (a) Calculated band structure of bulk HfS_3 perpendicular to the chain direction, that is, between Y and Γ points. The band structure indicates the hybridization between Hf-d (red) and S-p (blue) orbitals in the conduction band. Hf-p bands start to contribute significantly ~1.5 eV above the conduction band minimum. (b and c) Adjoining orbital resolved partial density of states corresponding to Hf (b) and S (c). The s orbital contribution is very small around the conduction and valence band edges.

strong Hf-weighted states at about 1.7 eV and 2.3 eV above the conduction band minimum. These intense XAS features result from very flat, minimally dispersing Hf-S hybrid states, as shown in Fig. 8.

For the Hf $4d_{5/2}$ absorption spectra, the two allowed transitions are d → p and d → f. The calculated band structure and partial density of states of HfS_3 shown in Fig. 8 indicate extensive S-p – Hf-d hybridization at the bottom of the conduction band minimum. Fig. 8b and c show that the unoccupied density of states within 1 eV above the conduction band minimum has almost equal contributions from Hf-d and S-p bands. The upper part of the conduction band from ~1.5 eV and above has significant contributions from Hf-p, Hf-s, and S-s bands. It is also worthwhile noting that the top of the valence band is predominantly formed by S-p contribution. Such an electronic structure of HfS_3 confirms that the features seen in the S core edge XAS spectrum originate from the transition from S 2p to the unoccupied S 3p – Hf 5d hybridized band. Here, the p–d hybridization of S and Hf, respectively, enables the S 2p → Hf 5d transition, circumventing the otherwise forbidden sulfur 2p → 3p transition. The fact that strong and significant band hybridization permits optical excitations to occur, which might otherwise be disallowed, has long been recognized.[59] This relaxation of some selection rules does not apply to symmetry restrictions imposed by the band symmetry as the optical excitations are strongly dichroic, as discussed above.

An in-depth study of TiS_3 and ZrS_3 found that the unoccupied states of the conduction band are dominated by sulfur p to transition metal d hybridization and, to a lesser extent, sulfur s to transition metal d hybridization,[39] consistent with previous predictions.[40] For HfS_3, this strong S 3p – Hf 5d hybridization in the conduction band is far more extensive and extends well above the conduction band minimum to far higher energies than seen for either TiS_3 or ZrS_3.[39]

Besides explaining the transitions in the XAS spectra, the calculated band structure also shows the origin of the theoretical indirect band gap of about 1.6 eV (Fig. 8a), which agrees with the experimentally observed indirect band gap of 2.0 eV (Fig. 4c) in the optical absorption.

3. Conclusions

In summary, this study reports on the electrical and optical properties of HfS_3 nanoribbons and provides some insight into their electronic structure. The optical absorption measurements indicate that HfS_3 has a direct optical band gap of about 2.3 eV and an indirect band gap of about 2.0 eV, which is supported by the calculated band structure. Based on the DFT results, both monolayered and few-layered HfS_3 crystals have direct and indirect band gaps that decrease with an increase in the number of layers. The DFT calculations, along with X-ray absorption spectroscopic studies of the unoccupied states, reveal that the conduction band minimum is formed by the hybridization of S 3p and Hf 5d levels, and it has a larger contribution from the S 3p in HfS_3 than in TiS_3 and ZrS_3. The temperature-dependent photoemission studies demonstrated negligibly small surface charging due to possibly highly mobile hole carriers or low recombination of the hole carriers generated during the photoemission process. The FET devices based on mechanically exfoliated few-layered HfS_3 nanoribbons exhibited strong dielectric behavior in the absence of light but showed n-type conductivity and a large photoresponse to

white light and several lasers with wavelengths in the visible range of the spectrum. The n-type characteristics were achieved when the HfS_3 FETs were studied in a vacuum, because if measured in air, the devices showed a p-type response, which is likely caused by physisorbed and chemisorbed oxygen species. The device photocurrent exhibited a strong dependence on the direction of polarization of the excitation laser, which is related to the highly anisotropic quasi-1D crystal structure of HfS_3. The results of this study suggest a potential application of HfS_3 in polarization-sensitive photodetectors.

4. Experimental

Synthesis of HfS_3

About 0.2 g of hafnium foil (Alfa Aesar, 99.9% metal basis excluding Zr; Zr – nominal 2%) and 0.3 g of sulfur powder (~15% excess relative to stoichiometric HfS_3; Alfa Aesar, 325 mesh, 99.999%) were sealed in a quartz ampoule under vacuum of about 200 mTorr. The ampoule was placed in a tube furnace, with one side of the ampoule located near the edge of the furnace to create a temperature gradient. The ampoule was annealed in a furnace at 650 °C for 14 days and then slowly cooled down. The excess of sulfur accumulated at the colder end of the ampoule, while millimeter long HfS_3 crystals were found on the hafnium foil and in some locations on the quartz surface. As discussed in our previous works,[23,55] HfS_3 is susceptible to surface oxidation, so the crystals were stored in a nitrogen glove box before the use.

Materials characterization

HfS_3 flakes were imaged using a FEI Tecnai Osiris scanning transmission electron microscope equipped with a HAADF detector and an X-FEG high-brightness Schottky field-emission gun. The accelerating voltage was 200 kV. For TEM characterization, a sample of HfS_3 was sonicated in ethanol for 2 min to separate small and thin crystals from the larger ones, and then the suspension was drop-cast on a lacey carbon-coated Cu TEM grid. SEM was performed using a Zeiss Supra 40 field-emission scanning electron microscope at an accelerating voltage of 5 kV. The XRD pattern of a HfS_3 powder was collected using a PANalytical Empyrean diffractometer in the Bragg–Brentano configuration with Ni-filtered Cu Kα radiation operated at 45 kV and 40 mA. Quantitative Rietveld refinement of the powder XRD pattern was performed using JANA2006 software,[60] employing internal tables for X-ray atomic form factors. AFM of HfS_3 flakes was performed using a Bruker Dimension Icon atomic force microscope in a tapping mode. UV-vis-NIR absorption spectra of a suspension of HfS_3 crystals in ethyl acetate were recorded using a Jasco V-670 spectrophotometer.

Device fabrication and electrical measurements

A Zeiss Supra 40 field-emission scanning electron microscope and a Raith pattern generator were used for electron beam lithography to pattern electrodes on HfS_3 flakes. An AJA electron beam evaporation system at a base pressure of $\sim 8 \times 10^{-9}$ Torr was used to evaporate 60 nm of Au at 2 nm s^{-1} rate. The HfS_3 devices were measured in a Lake Shore TTPX cryogenic probe station at a base pressure of about 2×10^{-6} Torr. After the evacuation, the devices were stored in a vacuum for at least two days before the measurements to minimize the effect of surface adsorbates on the electrical characteristics.[48] The probe station had a transparent window enabling optical excitation of HfS_3 devices that were electrically measured in a vacuum. The electrical measurements were performed using an Agilent 4155C semiconductor parameter analyzer. For the white light illumination, we used a 150 W Phillips 14501 DDL 20 V halogen light bulb. The emission spectrum of the bulb covered the entire visible range of the spectrum,[61] which was confirmed using an Ocean Optics USB2000 + XR1-ES spectrometer; the maximum light intensity at 600 nm was 6 mW cm^{-2}, which was measured using a Thorlabs S120C standard photodiode power sensor. For the wavelength-dependent photoconductivity measurements, we used a Thorlabs multichannel laser source with outputs at 685 nm (red), 520 nm (green), and 406 nm (blue) operated at the power of 5 mW and 0.5 mW. For the optical photoconductance anisotropy measurements, a laser beam was passed through a polarizer, and then the polarization angle φ was rotated using a half-wave plate; the rotation of the plate was performed using a Thorlabs K10CR1 stepper motor rotation mount.

X-ray photoemission spectroscopy (XPS)

The temperature-dependent XPS studies of the HfS_3 crystals were carried out to verify the existence of the photovoltaic effect at the surface of HfS_3. All the core level XPS measurements were carried out in an ultra-high vacuum chamber using a SPECS X-ray aluminum anode source ($h\nu$ = 1486.6 eV) and PHI Model: 10-360 hemispherical electron analyzer at different temperatures ranging from 180 K to 300 K by cooling down the sample using liquid nitrogen.

X-ray absorption spectroscopy (XAS)

The experiments on near-edge X-ray absorption fine structure spectroscopy (NEXAFS) of hafnium at the N_5 edge and sulfur at the L_3 and L_2 edges were performed at the Advanced Light Source bending magnet beamline 6.3.1 at the Lawrence Berkeley National Laboratory.[62] The XAS spectra were collected using the total electron yield (TEY) mode, where the compensation current from ground to the sample, which is proportional to the TEY from the sample, is recorded.

Computational details

The band structure of the HfS_3 bulk system and the element-based orbital resolved partial density of states of Hf and S were studied using DFT as applied in Vienna *ab initio* simulation package (VASP).[63,64] The electron–ion potential was approximated using the projected augmented plane wave (PAW) method.[65] The exchange and correlation potential was calculated using the generalized gradient approximation (GGA). In these calculations, we used a kinetic energy cutoff of 340 eV for the plane wave expansion of the PAWs and a $6 \times 8 \times 3$ grid of k points[66] for Brillouin zone integration. The exchange and

correlation, beyond GGA, were considered by introducing an onsite Coulomb repulsion with a Hubbard $U = 6.0$ eV for the Hf 5d orbitals in rotationally invariant formalism,[67] as implemented in VASP, to obtain matching of the calculated band gap. The electronic structure, however, was found to be qualitatively similar to those calculations carried out without the Hubbard U parameter. The van der Waals interaction was included in the calculations to describe the interlayer separation.[47] As HfS_3 is an n-type material, the Fermi level has been positioned at the conduction band minimum. DFT calculations of TiS_3 were previously found to provide very good agreement with the experimental band structure.[13] Also, the DFT approach that was employed here was successfully used elsewhere to describe the strong hybridization of chalcogen's p orbitals and transition metal's d orbitals in TiS_3 and ZrS_3.[39]

Author contributions

A. S. conceived the idea of this study. A. L. prepared HfS_3 devices and performed their electrical measurements. J. A. prepared HfS_3 crystals and performed XRD analysis, Raman spectroscopy, and UV-vis-NIR absorption spectroscopy. S. B. performed SEM and EDX mapping of HfS_3 crystals. M. J. L. performed AFM of HfS_3 flakes. K. A. and T. R. P. performed DFT calculations. G. V., A. D., T. K. E., E. M., and P. A. D. performed XPS of HfS_3 crystals and interpreted the results. G. V., M. Z., J. R., R. S., A. T. N., and P. A. D. performed XAS of HfS_3 crystals and interpreted the results. A. L., G. V., P. A. D., and A. S. wrote the manuscript. A. S. supervised the project.

Conflicts of interest

The authors declare no conflict of interest.

Acknowledgements

This work was supported by the National Science Foundation (NSF) through EPSCoR RII Track-1: Emergent Quantum Materials and Technologies (EQUATE), award OIA-2044049. A. L. acknowledges the support from the NSF, award OIA-1849206. T. R. P. acknowledges the support from the South Dakota Board of Regents, Competitive Research Grant 2021. This research used resources of the Advanced Light Source, which is a DOE Office of Science User Facility under contract no. DE-AC02-05CH11231. Some experiments were performed using the instrumentation at the Nebraska Nanoscale Facility, which is supported by the NSF, award ECCS-2025298, and the Nebraska Research Initiative.

References

1 J. O. Island, A. J. Molina-Mendoza, M. Barawi, R. Biele, E. Flores, J. M. Clamagirand, J. R. Ares, C. Sánchez, H. S. J. van der Zant, R. D'Agosta, I. J. Ferrer and A. Castellanos-Gomez, Electronics and optoelectronics of quasi-1D layered transition metal trichalcogenides, *2D Mater.*, 2017, **4**, 022003.

2 M. D. Randle, A. Lipatov, I. Mansaray, J. E. Han, A. Sinitskii and J. P. Bird, Collective states and charge density waves in the group IV transition metal trichalcogenides, *Appl. Phys. Lett.*, 2021, **118**, 210502.

3 A. A. Balandin, F. Kargar, T. T. Salguero and R. K. Lake, One-dimensional van der Waals quantum materials, *Mater. Today*, 2022, **55**, 74–91.

4 H. Haraldsen, E. Rost, A. Kjekshus and A. Steffens, On Properties of TiS_3, ZrS_3, and HfS_3, *Acta Chem. Scand.*, 1963, **17**, 1283–1292.

5 S. Furuseth, L. Brattas and A. Kjekshus, On the Crystal Structures of TiS_3, ZrS_3, $ZrSe_3$, $ZrTe_3$, HfS_3, and $HfSe_3$, *Acta Chem. Scand., Ser. A*, 1975, **29**, 623–631.

6 A. Lipatov, M. J. Loes, H. Lu, J. Dai, P. Patoka, N. S. Vorobeva, D. S. Muratov, G. Ulrich, B. Kästner, A. Hoehl, G. Ulm, X. C. Zeng, E. Rühl, A. Gruverman, P. A. Dowben and A. Sinitskii, Quasi-1D TiS_3 Nanoribbons: Mechanical Exfoliation and Thickness-Dependent Raman Spectroscopy, *ACS Nano*, 2018, **12**, 12713–12720.

7 J. O. Island, M. Buscema, M. Barawi, J. M. Clamagirand, J. R. Ares, C. Sánchez, I. J. Ferrer, G. A. Steele, H. S. J. van der Zant and A. Castellanos-Gomez, Ultrahigh Photoresponse of Few-Layer TiS_3 Nanoribbon Transistors, *Adv. Opt. Mater.*, 2014, **2**, 641–645.

8 A. Lipatov, P. M. Wilson, M. Shekhirev, J. D. Teeter, R. Netusil and A. Sinitskii, Few-layered titanium trisulfide (TiS_3) field-effect transistors, *Nanoscale*, 2015, **7**, 12291–12296.

9 J. O. Island, M. Barawi, R. Biele, A. Almazán, J. M. Clamagirand, J. R. Ares, C. Sánchez, H. S. J. van der Zant, J. V. Álvarez, R. D'Agosta, I. J. Ferrer and A. Castellanos-Gomez, TiS_3 Transistors with Tailored Morphology and Electrical Properties, *Adv. Mater.*, 2015, **27**, 2595–2601.

10 C. Huang, E. Zhang, X. Yuan, W. Wang, Y. Liu, C. Zhang, J. Ling, S. Liu and F. Xiu, Tunable charge density wave in TiS_3 nanoribbons, *Chin. Phys. B*, 2017, **26**, 067302.

11 A. J. Molina-Mendoza, J. O. Island, W. S. Paz, J. M. Clamagirand, J. R. Ares, E. Flores, F. Leardini, C. Sánchez, N. Agraït, G. Rubio-Bollinger, H. S. J. van der Zant, I. J. Ferrer, J. J. Palacios and A. Castellanos-Gomez, High Current Density Electrical Breakdown of TiS_3 Nanoribbon-Based Field-Effect Transistors, *Adv. Funct. Mater.*, 2017, **27**, 1605647.

12 A. Geremew, M. A. Bloodgood, E. Aytan, B. W. K. Woo, S. R. Corber, G. Liu, K. Bozhilov, T. T. Salguero, S. Rumyantsev, M. P. Rao and A. A. Balandin, Current Carrying Capacity of Quasi-1D $ZrTe_3$ van der Waals Nanoribbons, *IEEE Electron Device Lett.*, 2018, **39**, 735–738.

13 M. Randle, A. Lipatov, A. Kumar, C.-P. Kwan, J. Nathawat, B. Barut, S. Yin, K. He, N. Arabchigavkani, R. Dixit, T. Komesu, J. Avila, M. C. Asensio, P. A. Dowben, A. Sinitskii, U. Singisetti and J. P. Bird, Gate-Controlled Metal–Insulator Transition in TiS_3 Nanowire Field-Effect Transistors, *ACS Nano*, 2019, **13**, 803–811.

14 S. J. Gilbert, A. Lipatov, A. J. Yost, M. J. Loes, A. Sinitskii and P. A. Dowben, The electronic properties of Au and Pt metal

contacts on quasi-one-dimensional layered TiS_3(001), *Appl. Phys. Lett.*, 2019, **114**, 101604.
15 N. Papadopoulos, E. Flores, K. Watanabe, T. Taniguchi, J. R. Ares, C. Sanchez, I. J. Ferrer, A. Castellanos-Gomez, G. A. Steele and H. S. J. van der Zant, Multi-terminal electronic transport in boron nitride encapsulated TiS_3 nanosheets, *2D Mater.*, 2020, **7**, 015009.
16 M. D. Randle, A. Lipatov, A. Datta, A. Kumar, I. Mansaray, A. Sinitskii, U. Singisetti, J. E. Han and J. P. Bird, High-electric-field behavior of the metal-insulator transition in TiS_3 nanowire transistors, *Appl. Phys. Lett.*, 2022, **120**, 073102.
17 Y.-R. Tao, J.-J. Wu and X.-C. Wu, Enhanced ultraviolet-visible light responses of phototransistors based on single and a few ZrS_3 nanobelts, *Nanoscale*, 2015, **7**, 14292–14298.
18 X. Wang, K. Wu, M. Blei, Y. Wang, L. Pan, K. Zhao, C. Shan, M. Lei, Y. Cui, B. Chen, D. Wright, W. Hu, S. Tongay and Z. Wei, Highly Polarized Photoelectrical Response in vdW ZrS_3 Nanoribbons, *Adv. Electron. Mater.*, 2019, **5**, 1900419.
19 S. J. Gilbert, H. Yi, J.-S. Chen, A. J. Yost, A. Dhingra, J. Abourahma, A. Lipatov, J. Avila, T. Komesu, A. Sinitskii, M. C. Asensio and P. A. Dowben, Effect of Band Symmetry on Photocurrent Production in Quasi-One-Dimensional Transition-Metal Trichalcogenides, *ACS Appl. Mater. Interfaces*, 2020, **12**, 40525–40531.
20 V. V. Sysoev, A. V. Lashkov, A. Lipatov, I. A. Plugin, M. Bruns, D. Fuchs, A. S. Varezhnikov, M. Adib, M. Sommer and A. Sinitskii, UV-Light-Tunable p-/n-Type Chemiresistive Gas Sensors Based on Quasi-1D TiS_3 Nanoribbons: Detection of Isopropanol at ppm Concentrations, *Sensors*, 2022, **22**, 9815.
21 I. G. Gorlova and V. Y. Pokrovskii, Collective conduction mechanism in a quasi-one-dimensional TiS_3 compound, *JETP Lett.*, 2009, **90**, 295–298.
22 W.-W. Xiong, J.-Q. Chen, X.-C. Wu and J.-J. Zhu, Individual HfS_3 nanobelt for field-effect transistor and high performance visible-light detector, *J. Mater. Chem. C*, 2014, **2**, 7392–7395.
23 A. Dhingra, A. Lipatov, M. J. Loes, J. Abourahma, M. Pink, A. Sinitskii and P. A. Dowben, Effect of Au/HfS_3 interfacial interactions on properties of HfS_3-based devices, *Phys. Chem. Chem. Phys.*, 2022, **24**, 14016–14021.
24 W. Kong, C. Bacaksiz, B. Chen, K. Wu, M. Blei, X. Fan, Y. Shen, H. Sahin, D. Wright, D. S. Narang and S. Tongay, Angle resolved vibrational properties of anisotropic transition metal trichalcogenide nanosheets, *Nanoscale*, 2017, **9**, 4175–4182.
25 J. O. Island, R. Biele, M. Barawi, J. M. Clamagirand, J. R. Ares, C. Sánchez, H. S. J. van der Zant, I. J. Ferrer, R. D'Agosta and A. Castellanos-Gomez, Titanium trisulfide (TiS_3): a 2D semiconductor with quasi-1D optical and electronic properties, *Sci. Rep.*, 2016, **6**, 22214.
26 A. Pant, E. Torun, B. Chen, S. Bhat, X. Fan, K. Wu, D. P. Wright, F. M. Peeters, E. Soignard, H. Sahin and S. Tongay, Strong dichroic emission in the pseudo one dimensional material ZrS_3, *Nanoscale*, 2016, **8**, 16259–16265.
27 A. Khatibi, R. H. Godiksen, S. B. Basuvalingam, D. Pellegrino, A. A. Bol, B. Shokri and A. G. Curto, Anisotropic infrared light emission from quasi-1D layered TiS_3, *2D Mater.*, 2019, **7**, 015022.
28 N. Papadopoulos, R. Frisenda, R. Biele, E. Flores, J. R. Ares, C. Sánchez, H. S. J. Van Der Zant, I. J. Ferrer, R. D'Agosta and A. Castellanos-Gomez, Large birefringence and linear dichroism in TiS_3 nanosheets, *Nanoscale*, 2018, **10**, 12424–12429.
29 Z. Lian, Z. Jiang, T. Wang, M. Blei, Y. Qin, M. Washington, T.-M. Lu, S. Tongay, S. Zhang and S.-F. Shi, Anisotropic band structure of TiS_3 nanoribbon revealed by polarized photocurrent spectroscopy, *Appl. Phys. Lett.*, 2020, **117**, 073101.
30 S. Liu, W. Xiao, M. Zhong, L. Pan, X. Wang, H.-X. Deng, J. Liu, J. Li and Z. Wei, Highly polarization sensitive photodetectors based on quasi-1D titanium trisulfide (TiS_3), *Nanotechnology*, 2018, **29**, 184002.
31 Y.-R. Tao, J.-Q. Chen, J.-J. Wu, Y. Wu and X.-C. Wu, Flexible ultraviolet–visible photodetector based on HfS_3 nanobelt film, *J. Alloys Compd.*, 2016, **658**, 6–11.
32 L. Fan, Y. Tao, X. Wu, Z. Wu and J. Wu, HfX_3(X = Se and S)/graphene composites for flexible photodetectors from visible to near-infrared, *Mater. Res. Bull.*, 2017, **93**, 21–27.
33 E. Canadell, C. Thieffry, Y. Mathey and M. H. Whangbo, Energy factors governing the partial irreversibility of lithium intercalation in layered trichalcogenides MX_3 (M = Ti, Zr, Hf; X = S, Se) and the structural changes in the intercalated species Li_3MX_3, *Inorg. Chem.*, 1989, **28**, 3043–3047.
34 C. Sourisseau, Y. Mathey, I. Kerrache and C. Julien, Vibrational Study of Lithium Insertion and Bondings in Intercalated Li_3HfS_3 and $Li_{1.5}NiPS_3$ Semiconducting Phases, *J. Raman Spectrosc.*, 1996, **27**, 303–306.
35 E. Flores, J. R. Ares, I. J. Ferrer and C. Sánchez, Synthesis and characterization of a family of layered trichalcogenides for assisted hydrogen photogeneration, *Phys. Status Solidi RRL*, 2016, **10**, 802–806.
36 M. Li, J. Dai and X. C. Zeng, Tuning the electronic properties of transition-metal trichalcogenides via tensile strain, *Nanoscale*, 2015, **7**, 15385–15391.
37 Q. Zhao, Y. Guo, Y. Zhou, Z. Yao, Z. Ren, J. Bai and X. Xu, Band alignments and heterostructures of monolayer transition metal trichalcogenides MX_3 (M = Zr, Hf; X = S, Se) and dichalcogenides MX_2 (M = Tc, Re; X = S, Se) for solar applications, *Nanoscale*, 2018, **10**, 3547–3555.
38 N. S. Vorobeva, A. Lipatov, A. Torres, J. Dai, J. Abourahma, D. Le, A. Dhingra, S. J. Gilbert, P. V. Galiy, T. M. Nenchuk, D. S. Muratov, T. S. Rahman, X. C. Zeng, P. A. Dowben and A. Sinitskii, Anisotropic Properties of Quasi-1D In_4Se_3: Mechanical Exfoliation, Electronic Transport, and Polarization-Dependent Photoresponse, *Adv. Funct. Mater.*, 2021, **31**, 2106459.
39 S. J. Gilbert, H. Yi, T. Paudel, A. Lipatov, A. J. Yost, A. Sinitskii, E. Y. Tsymbal, J. Avila, M. C. Asensio and P. A. Dowben, Strong Metal–Sulfur Hybridization in the Conduction Band of the Quasi-One-Dimensional Transition-Metal Trichalcogenides: TiS_3 and ZrS_3, *J. Phys. Chem. C*, 2022, **126**, 17647–17655.

40 K. Taniguchi, Y. Gu, Y. Katsura, T. Yoshino and H. Takagi, Rechargeable Mg battery cathode TiS_3 with d–p orbital hybridized electronic structures, *Appl. Phys. Express*, 2016, **9**, 011801.
41 S. P. Gwet, Y. Mathey and C. Sourisseau, The Infrared, Raman, Resonance Raman Spectra, and the Valence Force Field of the HfS_3 Layer-Type Compound, *Phys. Status Solidi B*, 1984, **123**, 503–517.
42 H. Jin, D. Cheng, J. Li, X. Cao, B. Li, X. Wang, X. Liu and X. Zhao, Facile synthesis of zirconium trisulfide and hafnium trisulfide nanobelts: Growth mechanism and Raman spectroscopy, *Solid State Sci.*, 2011, **13**, 1166–1171.
43 F. Lyu, Y. Sun, Q. Yang, B. Tang, M. Li, Z. Li, M. Sun, P. Gao, L. H. Ye and Q. Chen, Thickness-dependent band gap of α-In_2Se_3: from electron energy loss spectroscopy to density functional theory calculations, *Nanotechnology*, 2020, **31**, 315711.
44 K. S. Novoselov, D. Jiang, F. Schedin, T. J. Booth, V. V. Khotkevich, S. V. Morozov and A. K. Geim, Two-dimensional atomic crystals, *Proc. Natl. Acad. Sci. U. S. A.*, 2005, **102**, 10451–10453.
45 Q. Cui, A. Lipatov, J. S. Wilt, M. Z. Bellus, X. C. Zeng, J. Wu, A. Sinitskii and H. Zhao, Time-Resolved Measurements of Photocarrier Dynamics in TiS_3 Nanoribbons, *ACS Appl. Mater. Interfaces*, 2016, **8**, 18334–18338.
46 J. Dai and X. C. Zeng, Titanium Trisulfide Monolayer: Theoretical Prediction of a New Direct-Gap Semiconductor with High and Anisotropic Carrier Mobility, *Angew. Chem., Int. Ed.*, 2015, **54**, 7572–7576.
47 S. Grimme, J. Antony, S. Ehrlich and H. Krieg, A consistent and accurate ab initio parametrization of density functional dispersion correction (DFT-D) for the 94 elements H-Pu, *J. Chem. Phys.*, 2010, **132**, 154104.
48 A. Sinitskii, A. Dimiev, D. V. Kosynkin and J. M. Tour, Graphene Nanoribbon Devices Produced by Oxidative Unzipping of Carbon Nanotubes, *ACS Nano*, 2010, **4**, 5405–5413.
49 A. Dhingra, A. Lipatov, A. Sinitskii and P. A. Dowben, Complexities at the Au/ZrS_3(001) interface probed by X-ray photoemission spectroscopy, *J. Phys.: Condens. Matter*, 2021, **33**, 434001.
50 S. Gilje, S. Han, M. Wang, K. L. Wang and R. B. Kaner, A chemical route to graphene for device applications, *Nano Lett.*, 2007, **7**, 3394–3398.
51 H. Wang, J. T. Robinson, X. Li and H. Dai, Solvothermal Reduction of Chemically Exfoliated Graphene Sheets, *J. Am. Chem. Soc.*, 2009, **131**, 9910–9911.
52 D. C. Marcano, D. V. Kosynkin, J. M. Berlin, A. Sinitskii, Z. Z. Sun, A. Slesarev, L. B. Alemany, W. Lu and J. M. Tour, Improved Synthesis of Graphene Oxide, *ACS Nano*, 2010, **4**, 4806–4814.
53 A. Sinitskii, D. V. Kosynkin, A. Dimiev and J. M. Tour, Corrugation of Chemically Converted Graphene Monolayers on SiO_2, *ACS Nano*, 2010, **4**, 3095–3102.
54 S. K. Srivastava and B. N. Avasthi, Preparation, structure and properties of transition metal trichalcogenides, *J. Mater. Sci.*, 1992, **27**, 3693–3705.
55 A. Dhingra, D. E. Nikonov, A. Lipatov, A. Sinitskii and P. A. Dowben, What happens when transition metal trichalcogenides are interfaced with gold?, *J. Mater. Res.*, 2023, **38**, 52–68.
56 J. Cazaux, Mechanisms of charging in electron spectroscopy, *J. Electron Spectrosc. Relat. Phenom.*, 1999, **105**, 155–185.
57 J. Cazaux, About the charge compensation of insulating samples in XPS, *J. Electron Spectrosc. Relat. Phenom.*, 2000, **113**, 15–33.
58 D. Pacilé, M. Papagno, M. Lavagnini, H. Berger, L. Degiorgi and M. Grioni, Photoemission and optical studies of $ZrSe_3$, $HfSe_3$, ZrS_3, *Phys. Rev. B: Condens. Matter Mater. Phys.*, 2007, **76**, 155406.
59 Y. Sakisaka, T. N. Rhodin and P. A. Dowben, Resonant photoemission at the 3s threshold of Ni, *Solid State Commun.*, 1984, **49**, 563–565.
60 V. Petříček, M. Dušek and L. Palatinus, Crystallographic Computing System JANA2006: General features, *Zeitschrift für Kristallographie – Crystalline Materials*, 2014, **229**, 345–352.
61 A. Lipatov, N. S. Vorobeva, T. Li, A. Gruverman and A. Sinitskii, Using Light for Better Programming of Ferroelectric Devices: Optoelectronic MoS_2-Pb(Zr,Ti)O_3 Memories with Improved On–Off Ratios, *Adv. Electron. Mater.*, 2021, **7**, 2001223.
62 P. Nachimuthu, J. H. Underwood, C. D. Kemp, E. M. Gullikson, D. W. Lindle, D. K. Shuh and R. C. C. Perera, Performance Characteristics of Beamline 6.3.1 from 200 eV to 2000 eV at the Advanced Light Source, *AIP Conf. Proc.*, 2004, **705**, 454–457.
63 G. Kresse and J. Furthmüller, Efficient iterative schemes for *ab initio* total-energy calculations using a plane-wave basis set, *Phys. Rev. B: Condens. Matter Mater. Phys.*, 1996, **54**, 11169–11186.
64 G. Kresse and D. Joubert, From ultrasoft pseudopotentials to the projector augmented-wave method, *Phys. Rev. B: Condens. Matter Mater. Phys.*, 1999, **59**, 1758–1775.
65 P. E. Blochl, Projector augmented-wave method, *Phys. Rev. B: Condens. Matter Mater. Phys.*, 1994, **50**, 17953–17979.
66 H. J. Monkhorst and J. D. Pack, Special Points for Brillouin-Zone Integrations, *Phys. Rev. B*, 1976, **13**, 5188–5192.
67 S. L. Dudarev, G. A. Botton, S. Y. Savrasov, C. J. Humphreys and A. P. Sutton, Electron-energy-loss spectra and the structural stability of nickel oxide: An LSDA + U study, *Phys. Rev. B: Condens. Matter Mater. Phys.*, 1998, **57**, 1505–1509.